

ENGINEERING

Three-dimensional perovskite nanowire array-based ultrafast resistive RAM with ultralong data retention

Yuting Zhang^{1,2†}, Swapnadeep Poddar^{1,2†}, He Huang³, Leilei Gu¹, Qianpeng Zhang^{1,2}, Yu Zhou¹, Shuai Yan⁴, Sifan Zhang⁴, Zhitang Song⁴, Baoling Huang³, Guozhen Shen⁵, Zhiyong Fan^{1,2,6,7,*}

Resistive random access memories (Re-RAMs) have transpired as a foremost candidate among emerging nonvolatile memory technologies with a potential to bridge the gap between the traditional volatile and fast dynamic RAMs and the nonvolatile and slow FLASH memories. Here, we report electrochemical metallization (ECM) Re-RAMs based on high-density three-dimensional halide perovskite nanowires (NWs) array as the switching layer clubbed between silver and aluminum contacts. NW Re-RAMs made of three types of methyl ammonium lead halide perovskites (MAPbX₃; X = Cl, Br, I) have been explored. A trade-off between device switching speed and retention time was intriguingly found. Ultrafast switching speed (200 ps) for monocrystalline MAPbI₃ and $\sim 7 \times 10^9$ s ultralong extrapolated retention time for polycrystalline MAPbCl₃ NW devices were obtained. Further, first-principles calculation revealed that Ag diffusion energy barrier increases when lattice size shrinks from MAPbI₃ to MAPbCl₃, culminating in the trade-off between the device switching speed and retention time.

INTRODUCTION

The dawn of neuromorphic computing, sophisticated bioelectronic modules, and big data analytics has accelerated the search for next-generation robust and nonvolatile memories (NVMs) (1, 2). In the past, resistive random access memories (Re-RAMs) have surfaced as promising NVMs because of their outstanding device scalability, multilevel data storage ability, ultrafast speed, excellent data retention (>10 years), and endurance performances (3–5). The conventional material choice for the switching layer of Re-RAMs includes metal oxides, i.e., NiO_x, SiO₂, Ta₂O₅, HfO₂, and CuO_x, while the emerging materials such as two-dimensional metal dichalcogenides are also being explored (2, 6, 7). Organic-inorganic hybrid perovskite materials with ABX₃ structures are traditionally famous in the genre of optoelectronic and photovoltaic devices. However, because of the innate hysteresis and innumerable charge/ion transport channels, these materials have started to be explored for Re-RAMs in the past few years. As the solvent engineering method of developing perovskite is compatible for fabricating flexible devices and because of the low cost of organic-inorganic hybrid perovskite materials, halide perovskite materials offer an opportunity for future embedded memories in wearable devices and large-scale industry applications (8–11). It is to be mentioned here that most of the traditional perovskite switching layers reported so far are in bulk thin-film form (12). A typical disadvantage of the thin film-based Re-RAMs include dearth of protection in environmentally delicate switching media (12, 13).

The problem becomes more acute in organic-inorganic hybrid perovskite Re-RAMs that suffer from moisture attack and quick degradation, which, in turn, notably suppresses the figure of merits (FOMs) and performance metrics. Thin film-based switching media also thwarts effective integration of multiple Re-RAM cells in a single chip due to the presence of potential horizontal pathways facilitating electrical leakage (14). In this regard, electrically isolated nanowire (NW) Re-RAMs hold promise for high device integration density. Among the NW-based memory cells, most reports involve horizontal NWs that hinder large-scale assembly and full-scale performance utilization in memory cells (15, 16). In addition, the fewer reports on vertical NW Re-RAMs do not incorporate any protective engineering to prevent the lateral leakage and material stability problems (17). Therefore, it is of utmost necessity that a switching layer anatomy in Re-RAMs is deciphered such that the concerning issues regarding material stability of environmentally sensitive materials like perovskite, adjacent electrical leakages and NW assembly, can be addressed effectively and in conjunction.

Recently, we have reported that nanoengineered porous alumina membrane (PAM) can serve as a highly efficacious protecting template to substantially improve the stability of perovskite NWs for high-performance optoelectronics owing to its ability to hinder the surface diffusion pathways of absorbed moisture and oxygen (13, 18). In this work, we demonstrated electrochemical metallization (ECM)-based Re-RAMs comprising arrays of three-dimensionally integrated methyl ammonium lead halide perovskite (MAPbX₃; X = Cl, Br, I) NWs embedded in a nanoengineered PAM as the switching medium with an NW integration density as high as 10⁸ to 10⁹ cm⁻² and almost 100% fill ratio. By punctilious and methodical studies to explore MAPbCl₃ NWs in the PAM template as the switching layer, we were able to achieve the data retention performance to $\sim 9 \times 10^8$ s for vapor-solid-solid reaction (VSSR) grown MAPbCl₃ monocrystalline NWs and to $\sim 7 \times 10^9$ s for solvent engineering-based polycrystalline NWs, at room temperature, as observed from extrapolated temperature-dependent Arrhenius plots. Our real-time continuous room temperature measurements also confirmed data retention capability greater than 10⁷ s without any perceptible degradation of the resistance states. To the best of our knowledge, this data

¹Department of Electronic and Computer Engineering, The Hong Kong University of Science and Technology, Clear Water Bay, Kowloon, Hong Kong SAR, China.

²Guangzhou HKUST Fok Ying Tung Research Institute, Nansha, Guangzhou 511458, China. ³Department of Mechanical and Aerospace Engineering, The Hong Kong University of Science and Technology, Clear Water Bay, Hong Kong SAR, China.

⁴State Key Laboratory of Functional Materials for Informatics, Shanghai Institute of Micro-system and Information Technology, Chinese Academy of Sciences, Shanghai 200050, China. ⁵State Key Laboratory for Superlattices and Microstructures, Institute of Semiconductors, Chinese Academy of Sciences, Beijing 100083, China.

⁶Guangdong-Hong Kong-Macao Intelligent Micro-Nano Optoelectronic Technology Joint Laboratory, The Hong Kong University of Science and Technology, Clear Water Bay, Kowloon, Hong Kong SAR, China. ⁷HKUST-Shenzhen Research Institute, No. 9 Yuexing First RD, South Area, Hi-tech Park, Nanshan, Shenzhen 518057, China.

*Corresponding author. Email: eezfan@ust.hk

†These authors contributed equally to this work.

retention performance is the longest among all organic-inorganic hybrid perovskite Re-RAM systems reported so far (19–27). Our Ag/MAPbCl₃ NWs/Al Re-RAM devices also exhibited fast erasing and writing speed of 300 and 800 ps, respectively, ON/OFF ratio of $\sim 10^7$, and endurance of 3×10^6 cycles. A systematic study has been carried out on Ag/MAPbX₃ NWs/Al Re-RAM devices; the performance parameters of MAPbCl₃ NWs were compared to their iodide and bromide siblings (MAPbI₃ and MAPbBr₃). A trade-off between retention time and speed has been observed for MAPbCl₃, MAPbBr₃, and MAPbI₃, respectively. Overall, the chloride-based system exhibited the best retention time, and the iodide one showed the fastest operational speed (200 ps). To gain in-depth understanding, Vienna Ab initio Simulation Package (VASP) with the predicted augmented wave approach was used to explain this trade-off between speed and retention time. In short, higher energy barrier for Ag diffusion, smaller lattice spacing, and stronger bonding in MAPbCl₃ were found to be responsible for the relatively longer retention time and slower speed when compared to other halide perovskite systems. Also, the polycrystalline NWs have even higher diffusion energy barrier and more grain boundaries further assist Ag clusters' trapping when compared to monocrystalline NWs, which explains the ~ 8.2 times improvement of data retention performance at room temperature for MAPbCl₃ NWs. The overall improvement of material stability and hence retention ability and endurance compared to the thin-film counterparts were attributed to the excellent lateral passivation provided by the PAM walls and the epoxy packaging on the top.

RESULTS

The device structure is shown in Fig. 1A. The switching layer is composed of MAPbCl₃ NWs planted in the PAM, sandwiched between

silver (Ag) and aluminum (Al) contacts acting as the active electrode (AE) and counter electrode (CE), respectively. PAM was used as a template for NWs' growth and provided surface passivation. The NWs were grown by a bottom-up VSSR process as reported previously by us (28–30). The diameter of the NWs was ~ 250 nm, and they demonstrated integration density as high as 4×10^8 cm⁻². The cross-sectional images of the MAPbCl₃ NWs rooted in the PAM and with length ~ 1 μ m are shown in Fig. 1B. The NWs in the PAM exhibited close to 100% filling as shown in figs. S1 and S2, which ensures 100% of yield for device switching behavior (fig. S3). As shown in Fig. 1C, most planes of the MAPbCl₃ NWs [(100) being predominant] in the x-ray diffraction (XRD) pattern match that of standard cubic MAPbCl₃, thereby indicating a perfect cubic crystal structure (31). Figure 1D represents the typical current-voltage (*I-V*) characteristics of MAPbCl₃ NW-based Re-RAM. A dc voltage sweep of 0 \rightarrow +8 V \rightarrow 0 V \rightarrow -8 V \rightarrow 0 V was applied to the device with 0.1-A current compliance (CC) to prevent the device from breakdown. The device exhibited abrupt SET and RESET at threshold switching voltage of 3 and -2.5 V, respectively. The switching behavior in perovskite-based Re-RAM with Ag as the active electrode is attributed to ECM of Ag, resulting in inhomogeneous filament formation as has been explored (25, 32–34). Furthermore, as shown in fig. S4, the higher atomic percentage of Ag in switched NWs (SNWs) as compared to unswitched ones [pristine NWs (PNWs)] bears evidence of the Ag permeation. The PNWs showed no detectable trace of Ag inside. Scanning electron microscopy (SEM) and energy-dispersive x-ray spectroscopy (EDS) characterization of the top and bottom view of MAPbCl₃ NWs array shown in figs. S5 and S6 also confirmed the Ag filament's existence in the NW bulk. Specifically, SNWs and PNWs were made to undergo comparative EDS, which revealed that only the SNWs had mapped traces of Ag

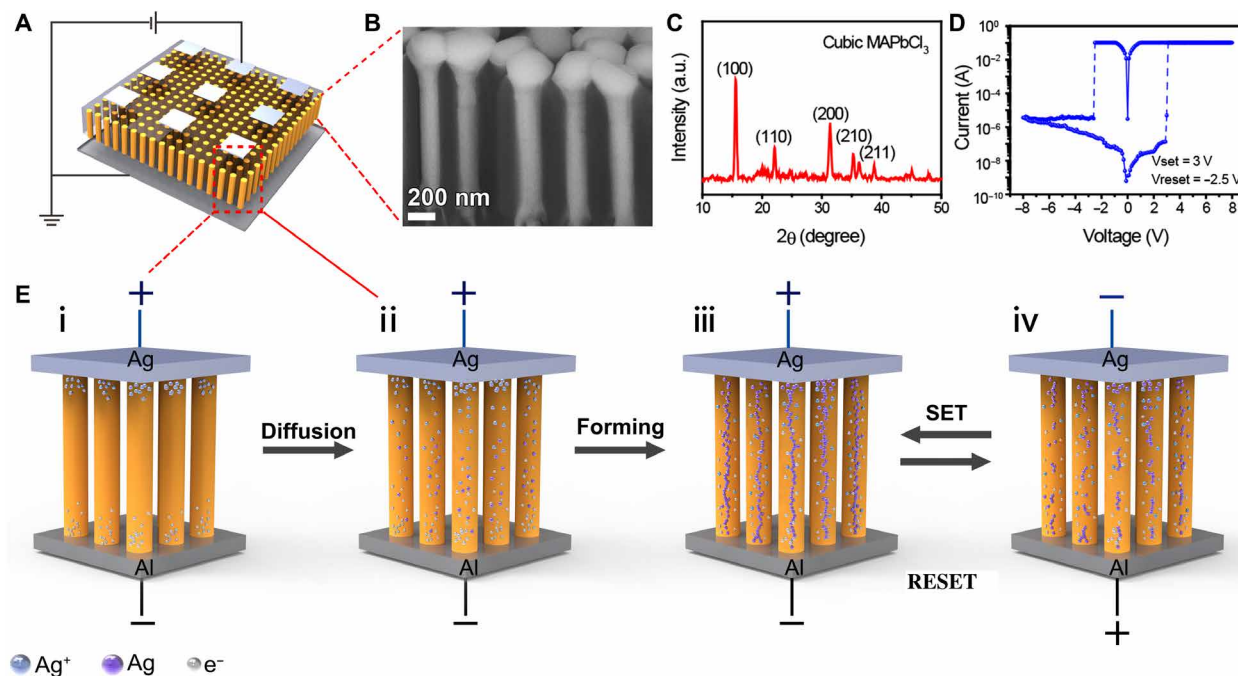


Fig. 1. Device structure analysis and working mechanism of MAPbCl₃ NW-based device. (A) Device schematic of MAPbCl₃ NWs in the PAM template with Ag as active electrode and Al as counter electrode. (B) Cross-sectional SEM image of MAPbCl₃ NWs in PAM. (C) XRD characterization of MAPbCl₃ NWs. a.u., arbitrary units. (D) *I-V* characteristics of Ag/MAPbCl₃ NWs/Al Re-RAM devices. (E) Working mechanism of Ag/MAPbCl₃ NWs/Al Re-RAM devices.

that was driven in while switching. Qualitatively, it was also observed that the Ag concentration within the NWs was more near the top contact electrode as compared to the bottom contact electrode. Furthermore, fig. S7 shows the comparative XRD peak analysis of MAPbCl₃ SNWs and PNWs. The SNWs demonstrated an Ag peak representing (111) plane, although no such peak was visible in the PNWs. On the basis of the above findings, we reveal an ECM mechanism that was instrumental in causing the resistive switching behavior in our perovskite Re-RAM. Figure 1E shows the schematic of the SET and RESET mechanism. When positive voltage is applied to Ag electrode, Ag atoms are oxidized into Ag⁺ ions and then intrude into the NWs. Driven by the external electric field, the incoming Ag⁺ ions move toward the mobile electrons coming from the Al CE. Then, these ions are subsequently reduced near the CE and elsewhere in the body of the NWs. Further nucleation and electrocrystallization would trigger the filament growth, and ultimately, the AE and CE would be connected by metallic silver bridge/s (35). The formation of the bridge results in the low resistance state (LRS). The LRS is retained until opposite polarity voltage and consequent dominant Joule's heating rupture the Ag bridge and the system ultimately goes back to the high resistance state (HRS) (33).

Multilevel resistance states provide the possibility of ultrahigh data storage density because multiple resistance states corresponding to multiple bits can be stored in a single memory cell. The large ON/OFF ratio of $\sim 10^7$ as obtained in the MAPbCl₃ NWs (see Fig. 1D) presents us a large reading window for the many resistance levels. It has been reported previously that the CC is one of the

pivotal factors influencing the formation of filaments. A larger SET CC would result in a more robust filament and a lower resistance level compared to a lower SET CC (32, 36). Here, six distinct LRSs were obtained from our Ag/MAPbCl₃ NWs/Al Re-RAM devices by controlling with different SET CCs ($CC = 10^{-6}$, 10^{-5} , 10^{-4} , 10^{-3} , 10^{-2} , and 10^{-1} A), while a single HRS was observed as shown in Fig. 2A. Each data point of the LRSs represents a resistance level obtained from the SET process of standard *I-V* characterization. Eight such SET cycles were run for each LRS, and it is well observed that the LRSs are distinctly distinguishable from one another, indicating excellent data fidelity. Correspondingly, the HRS values were obtained from a standard *I-V* characterizations after the completion of the SET/RESET process. The *I-V* characterization with different compliances has been shown in fig. S8. Switching endurance is another very important FOM for demonstrating reliability of memory devices. Figure 2B shows the endurance study of Ag/MAPbCl₃ NWs/Al Re-RAM devices that is measured by applying ac voltage pulse sequences comprising 0.5/9/0.5/−9/−0.5-V pulses and 100- μ s pulse duration. The cyclic endurance can reach up to 3×10^6 cycles without any degradation in the ON/OFF ratio. For a comprehensive statistical study, 18 devices were measured to demonstrate the device-to-device variation as shown in fig. S9, with a mean endurance value of $\sim 10^6$ cycles. The excellent endurance performance can be attributed to the material stability induced by electrical isolation of the PAM walls and the surface passivation provided by the NOA81 epoxy surface packaging. Figure 2C shows the Ag/MAPbCl₃ NWs/Al Re-RAM devices' reliability in an ambient environment and

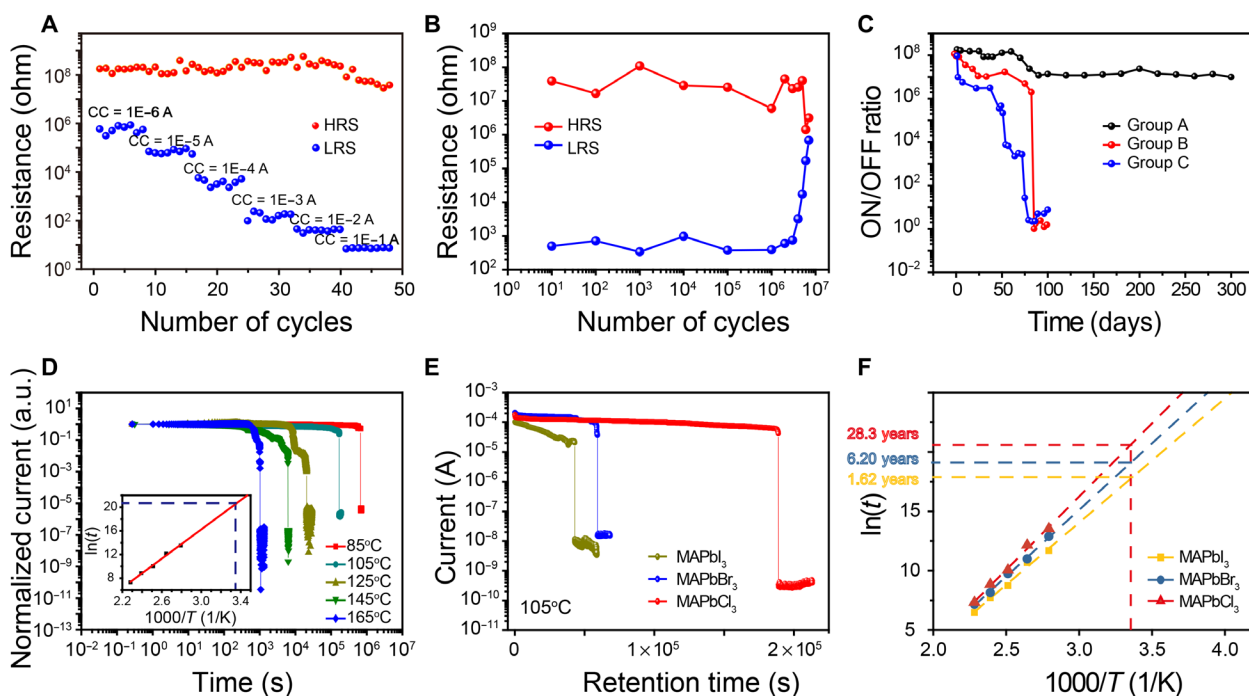


Fig. 2. Electrical characterization, multibit storage, and data retention of MAPbX₃ NW-based Re-RAM devices. (A) Multilevel resistance states of Ag/MAPbCl₃ NWs/Al Re-RAM devices with different current compliances. (B) Switching endurance performance of Ag/MAPbCl₃ NWs/Al Re-RAM devices. (C) Reliability test of the Ag/MAPbCl₃/Al Re-RAM devices in an ambient environment and 85°C/80% RH condition. Group A: Ag/MAPbCl₃ NW/Al Re-RAM device at ambient environment. Group B: Ag/MAPbCl₃ NW/Al Re-RAM device at 85°C and 80% RH. Group C: Ag/MAPbCl₃ thin-film/Al Re-RAM device at 85°C and 80% RH. (D) ON state retention time measurement of Ag/MAPbCl₃ NWs/Al Re-RAM devices at different temperature. Inset: $\ln(t)$ -1000/T plot. Retention time at room temperature (RT) was extrapolated from the linear fitting. (E) Retention performance measured at 105°C of MAPbI₃, MAPbBr₃, and MAPbCl₃ NW-based Re-RAM devices. All the NWs are 1 μ m in length. (F) $\ln(t)$ -1000/T plot of MAPbX₃-based Re-RAM devices.

85°C/80% relative humidity (RH) environment. The ON/OFF ratio was obtained from the standard I - V scan characterization. The devices maintained $\sim 10^7$ ON/OFF ratio for more than 300 days in ambient environment. The ON/OFF ratio of devices at 85°C and 80% RH degraded much faster than that in ambient condition. However, the devices can still maintain a $\sim 10^6$ ON/OFF ratio beyond 85 days (~ 2000 hours). A batch of Ag/MAPbCl₃ thin-film/Al Re-RAM devices was fabricated for comparing with the NW-based devices. SEM images of MAPbX₃ thin film at different temperature are shown in fig. S10. They could only maintain a high ON/OFF ratio for 37 days at 85°C and 80% RH environment with epoxy packaging. The Ag/MAPbCl₃ NWs/Al Re-RAM devices exhibited outstanding reliability not only in ambient environment but also in a high-temperature and high-humidity environment. One of the key FOMs of NVMs is its temporal data retention ability. Up until now, perovskite Re-RAMs have not shown promising performance as far as retention ability is concerned (23). Here, we have carried out rigorous retention time study by exploring device failure at elevated temperature and obtaining the extrapolated data retention time from Arrhenius plots. The devices under test were placed on the mounting stage of the probe station at individual temperature in the inception for ~ 15 min to obtain a uniform and stable temperature distribution on the device. For data retention ability, as the SET voltage and the readout voltage bias affect the device performance, the readout voltage should be substantially smaller than the SET voltage to ensure sufficient immunity against pseudo-SET under prolonged readout biasing (1). In our retention time measurement system, a positive half of the I - V scan ($0 \rightarrow 8 \text{ V} \rightarrow 0 \text{ V}$) with 0.1-A CC was used to switch the devices from HRS to LRS. Afterward, a constant 10-mV reading voltage was applied to monitor the resistance of the Re-RAM devices. Figure 2D shows the retention time of Ag/MAPbCl₃ NWs/Al Re-RAM devices measured at 85°, 105°, 125°, 145°, and 165°C. We defined the normalized current as the ratio between the instantaneous current and the initial current. For Ag filament-based Re-RAM, the retention time is determined by Ag diffusion after the Ag filament is formed. The Ag diffusion process is thermally activated and follows the Arrhenius relationship. The retention time (t) decreased with the increase of temperature and followed the Arrhenius relation [$\ln(t) \propto E_a/kT$], where E_a is the activation energy of Ag diffusion in the crystal, k is the Boltzmann constant, and T is the absolute temperature (37). Activation energy (E_a) extraction by the Arrhenius method in the retention plot is a technique used ubiquitously to estimate data retention (37–44). However, for perovskite Re-RAM devices, in the past, researchers have rarely used this method to identify the real retention time of devices, mainly because of the material and thermal stability issue plaguing the perovskite thin films (as shown in fig. S10). Hence, mostly reported retention data were obtained at room temperature. Here, in this work, the material stability issue concerning perovskite has been addressed by using nanoengineered PAM to protect the embedded perovskite NWs. The perovskite stability could be preserved in the PAM without any epoxy encapsulation for more than 7 months, which was reported by us previously (29). In addition, the growth temperature of the perovskite NWs was 180°C in the VSSR process (see Materials and Methods), and recently, we also reported that the PAM has higher thermal conductivity than the perovskite NWs, which instills thermal stability to the NWs by assisting with heat dissipation (18). Therefore, after the alleviation of the thermal stability issue using PAM, the temperature expedited Arrhenius extrapolation method

could be used by us effectively to ascertain the estimated retention time of perovskite NW Re-RAMs. The inset plot in Fig. 2D shows the Arrhenius fitting curve and the subsequent extrapolated data retention time of 9×10^8 s at room temperature. The activation energy (E_a) was extracted to be 1.07 eV, which is in congruence with Ag diffusion activation energy value reported before for other switching media (37, 45). Similar retention failure plots for MAPbI₃ and MAPbBr₃ NW-based Re-RAM are shown in fig. S11. Intriguingly, we found that MAPbCl₃ NW-based devices exhibited the longest retention time and highest activation energy. Figure 2E shows the retention time of MAPbX₃ (X = Cl, Br, I) NW-based Re-RAM at 105°C. The devices exhibited excellent retention capability at high temperature, which reaffirms the possibility of using these devices in practical electronic devices involving thermally rugged ambience. As observed from Fig. 2F, the slope of the Arrhenius fitting curve, i.e., the activation energy of Ag diffusion in MAPbI₃, MAPbBr₃, and MAPbCl₃ crystals, gradually increases as 0.90, 0.97, and 1.07 eV, respectively. The estimated retention time at room temperature extracted out from the fitting curves was found to be 1.62, 6.20, and 28.3 years, respectively. For MAPbCl₃ NW-based Re-RAM, real-time nonextrapolated measurement yielded retention time beyond 10^7 s at room temperature without perceptible data degradation as shown in fig. S12. It must be mentioned here that the extrapolated retention time portrays the theoretical upper limit of retention performance of the device. However, the device lifetime would play a critical role in ascertaining the retention ability of the device. That is an area of research that we plan to focus on in the future.

To delve deep into the intrinsic mechanism guiding the remarkable data retention ability of MAPbCl₃ NW-based Re-RAM, we carried out simulations based on density functional theory (DFT). Supercells ($2 \times 2 \times 2$) of the CH₃NH₃PbX₃ (MAPbX₃; X = Cl, Br, or I) perovskite structures were used for the structural optimization and further for distinct Ag doping cases, as shown in Fig. 3A. For the Ag doping cases, two different Ag insertion levels were considered, namely, the Ag_{0.5}MAPbX₃ and AgMAPbX₃ perovskite structures. The structural optimizations were adopted by using similar critical conditions. The single Ag atom diffusion pathway and transitional configurations in the Ag_{0.5}MAPbX₃ and AgMAPbX₃ perovskite structures are shown in Fig. 3 (B and C). A total of nine pixels were adopted to compute the total energy difference between the transitional states to find a minimum energy pathway. The crystalline morphology of the perovskite structures remained as it is with small lattice expansion when the Ag insertion levels are stoichiometrically 0.5 and 1. The activation energy simulation result is shown in Fig. 3 (D and E). The E_a values of Ag atoms are 0.61 to 0.64 eV in MAPbI₃ crystal structure, 0.79 to 0.85 eV in MAPbBr₃ crystal structure, and 0.91 to 1.04 eV in MAPbCl₃ crystal structure. In different Ag concentrations (Ag/Pb = 0.5 and Ag/Pb = 1), the simulation result shows the same trend that Ag atoms have the largest diffusion barrier energy in MAPbCl₃ crystal structure, which works in concurrence with our experimental results. For the difference between the simulation results and the experimental value, PAM confinement for NWs in the experiment scenario can be an important reason. It has been widely studied that the strain and volume confinement have significant influence on the diffusion energy barrier. Volume confinement and compressive strain can lead to higher activation energy (46, 47). There are three main reasons contributing to the difference of activation energy and hence the retention time

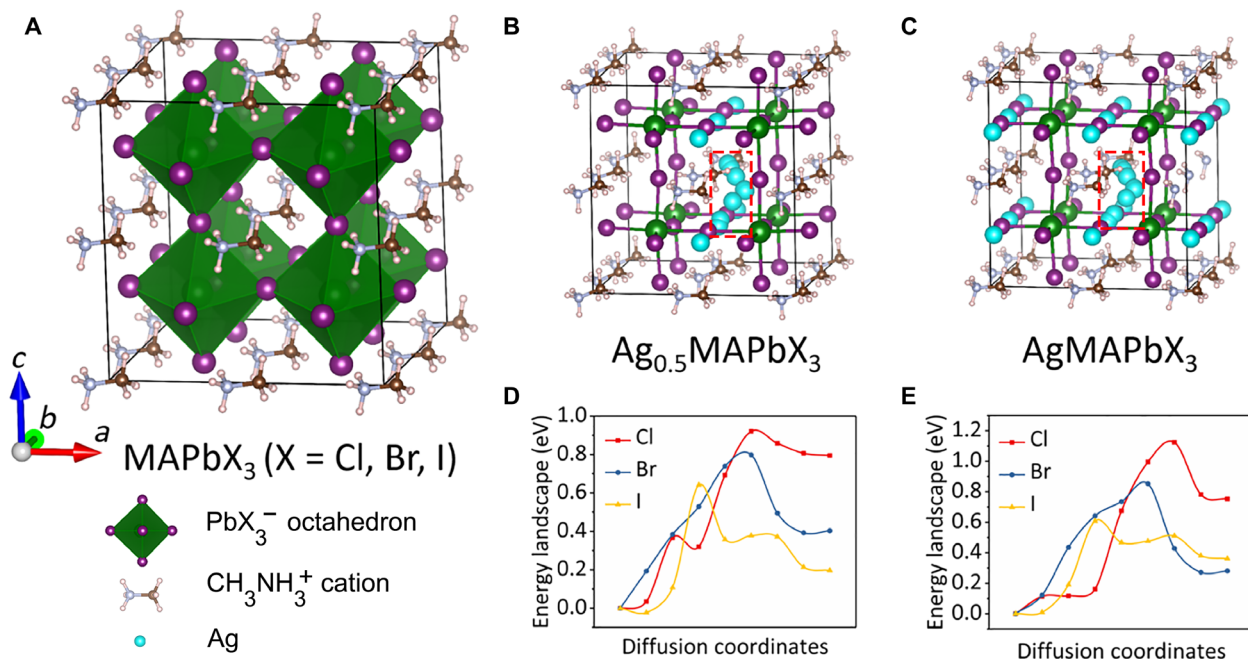


Fig. 3. Activation energy simulation based on MAPbX₃ crystal structure. (A) Optimized 2 × 2 × 2 perovskite supercell of CH₃NH₃PbX₃ (X = Cl, Br, or I). Methyl-ammonium (CH₃NH₃⁺) cation occupies the central site surrounded by 12 nearest neighbor halide ions in eight corner-sharing PbX₃⁻ octahedra. (B and C) Single Ag atom diffusion pathway and transitional configurations in the Ag_{0.5}MAPbX₃ and AgMAPbX₃ perovskite structures. The selected part represents the NEB path of Ag diffusion from a one stable site to a nearby stable site. (D and E) Corresponding energy landscape of single Ag atom diffusion from its initial stable site to the next stable site.

among different MAPbX₃. First, the lattice parameters have an instrumental role to play. The MAPbCl₃ crystal structure occupies the smallest lattice parameters because of the smallest radii of chlorine atoms [MAPbCl₃ ($a = 5.68 \text{ \AA}$) versus MAPbI₃ ($a = 6.28 \text{ \AA}$) and MAPbBr₃ ($a = 5.90 \text{ \AA}$)] (48). On the basis of the reversible switching behavior, the Ag atoms are supposed to occupy the interstitial sites of cubic crystal structure. Larger crystal parameters promise a large space for Ag atoms' diffusion and lower energy barrier, as well as faster switching speed. Second, the bonding energy of Pb-Cl is larger than Pb-Br and Pb-I, which indicates that MAPbCl₃ has better chemical stability than other two (49). The electronegativity that increases in the order of I < Br < Cl also contributes to stronger bonding energy of Pb-Cl. In addition, the bonding energy of Pb-Cl is larger than Ag-Cl, indicating that Ag atoms are less prone to have electrochemical reaction with MAPbCl₃ matrix. However, the condition reverses in the other two systems, again showing that the MAPbCl₃ system is the most stable one. After the filament is properly formed, a stable host environment would help to maintain the filament and prolong the retention time. Last, according to previous reports, MAPbX₃ crystal structures' tolerance factor varies between 0.9 and 1, increasing progressively in the sequence of MAPbI₃, MAPbBr₃, and MAPbCl₃. In this range, the crystal structure is closer to a perfect and stable cubic crystal structure when the tolerance factor is closer to 1 (50). Hence, the MAPbCl₃ system is supposed to render the most steady crystal structure. All these three reasons as mentioned above make MAPbCl₃ NWs the best candidate for demonstration of superior data retention ability in NVMs, when compared to the iodide and bromide counterparts. Coupled with all of these, the lateral PAM passivation and NOA81 epoxy sheath on the top provides the MAPbX₃ NW advantage in terms of temporal data storage over previously reported thin-film perovskite Re-RAMs that lack

these ammunitions to defend against atmospheric moisture. To further reaffirm the claim, we also measured the thin-film MAPbCl₃ devices that showed retention time of only 1923 s compared to 749,675-s data retention at 85°C for our NW-based devices (see fig. S13).

Logically, a higher diffusion barrier should hinder a faster switching process. In this work, we systematically studied the switching speed of MAPbX₃ (X = Cl, Br, I)-based Re-RAM devices. A single pulse with duration from 100 ps to 1 ns was applied to the devices. The singular pulses of different duration as provided by the picosecond pulse generator and observed by an oscilloscope are shown in fig. S14. The resistances of the devices were monitored by a source meter every time before and after the application of the single pulse. The reading voltage was 0.1 V to ascertain the value of the devices' resistances. An *I-V* curve comparison study of Ag/MAPbX₃/Al Re-RAM devices was shown in fig. S15; devices with higher diffusion barrier and longer NWs length required larger set voltage. To substantially reduce the transit path of the electrons and moving ions within the NW, we used NW length as short as 200 nm (diameter of ~15 nm) to demonstrate the operating speed performance for our Re-RAM devices. Figure 4 depicts that devices with 200-nm length can all be SET and RESET by single pulse with duration less than 1 ns. MAPbI₃ NW-based devices exhibited fastest switching among three kinds of devices with 200-ps SET speed and 200-ps RESET speed. Figure 4A shows that Ag/MAPbI₃ NWs/Al-based devices can be SET from HRS to LRS under the condition of applying a single pulse with pulse duration of and beyond 200 ps. When the pulse width increased from 200 to 400 ps, the SET voltage decreased from 4.1 to 1.7 V. For the RESET process shown in Fig. 4B, the device can be RESET from LRS to HRS by single pulse with duration of and larger than 200 ps. Akin to the SET process, pulses with large

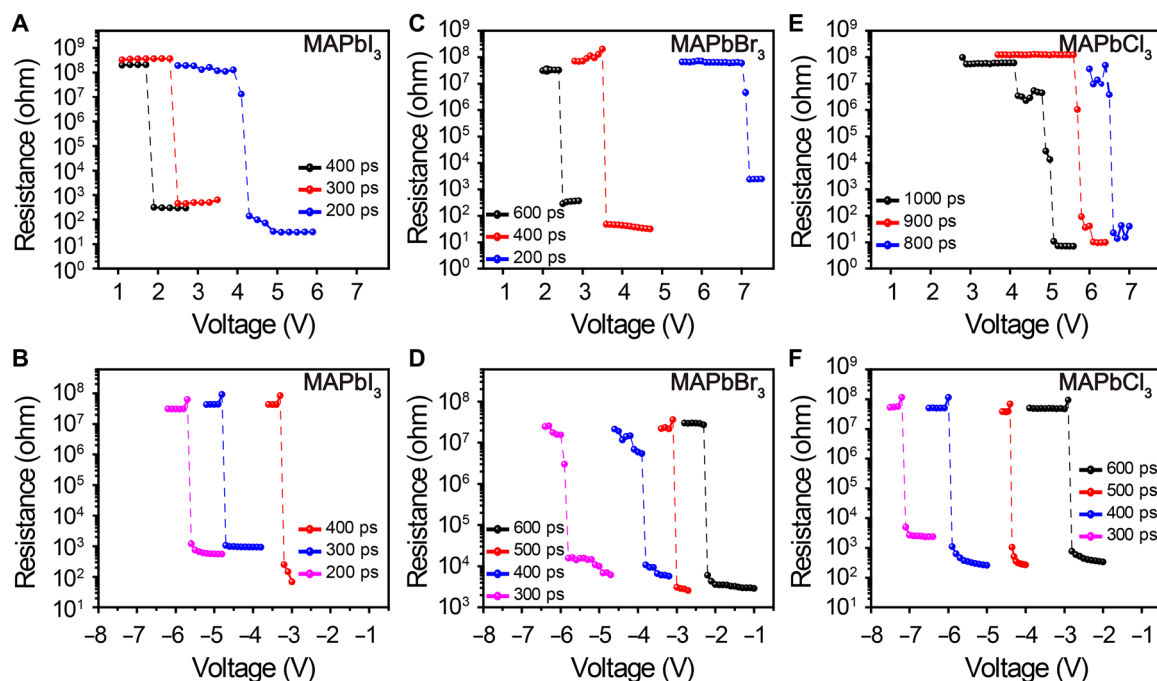


Fig. 4. Switching speed characterization of 200-nm-long MAPbX₃ NW-based devices. (A) Writing speed and (B) erasing speed measurements for MAPbI₃-based device. (C) Writing speed and (D) erasing speed measurements for MAPbBr₃-based device. (E) Writing speed and (F) erasing speed measurement for MAPbCl₃-based device.

pulse duration resulted in lower RESET voltage. Figure 4 (C to F) shows that MAPbBr₃-based devices could reach a 200-ps SET speed and 300-ps RESET speed, while MAPbCl₃-based devices could reach 800-ps SET speed and 300-ps RESET speed. However, MAPbBr₃-based devices required higher operation voltage than MAPbI₃-based devices when switched with the pulse of the same width, e.g., MAPbBr₃-based devices switched at 7.1 V and MAPbI₃-based devices switched at 4.1 V for 200-ps pulse during the SET process. MAPbCl₃-based devices exhibited similar increasing trend of threshold voltage when compared to MAPbBr₃ and MAPbI₃ devices for the same switching pulse width. The intriguingly fast operational speed of perovskite NW-based Re-RAMs can be attributed to the highly mobile electrons in the monocryalline NWs reducing the fast moving Ag⁺ ions within the body of the NWs. Also, the shorter is the length of the NW, the shorter is the distance that the electrons and the Ag⁺ ions have to travel before Ag⁺ ion reduction and filament initiation or rupture occur. To the best of our knowledge, the thin-film thicknesses of amorphous nitride- and oxide-based Re-RAMs exhibiting subnanosecond switching are all below 10 nm (51–54). Intrinsically, when compared to those traditional material systems, our perovskite NW devices might have faster switching speed, if using the same thickness. This is due to the fact that ionic and electronic mobilities are much higher in any semiconducting media compared to amorphous ones. When comparing the fastest speed among the three MAPbX₃ systems in concern, MAPbCl₃ crystal is supposed to have the highest activation energy that contributes to the longest data retention time but the slowest switching speed. This is because the higher the activation energy is, the more difficult it will be for the Ag to migrate in the NWs and therefore will require higher switching threshold voltage. There is always a trade-off between switching speed and retention time, and hence, there is always a

window for device engineers to explore and build a system based on their requirements. It must also be mentioned here that if the subnanosecond switching speed is taken into consideration for estimating switching energy per bit, the energies are in the ~pJ range, which is comparable with the state-of-the-art standard for all Re-RAMs.

To further demonstrate the aforementioned influence of activation energy on retention time, we used solvent engineering method to enhance the activation energy of Ag atoms diffusing in MAPbCl₃ crystals. The device fabrication by solvent engineering method is based on spin coating and annealing (see Materials and Methods). High-resolution transmission electron microscope (HRTEM) images and fast Fourier transform analysis were used to ascertain the crystalline nature of MAPbCl₃ NWs obtained by solvent engineering and VSSR growth. To characterize the crystal lattice successfully, NWs with ~15 nm diameter were used in the TEM characterization for both solvent engineering method and VSSR growth. Figure 5 (A and B) shows that NWs fabricated by solvent engineering method are polycrystalline, the crystal lattice orientated in varying directions, while Fig. 5 (C and D) shows that those fabricated by the VSSR process are monocryalline. The grain boundary of polycrystalline NWs can increase the diffusion barrier energy of Ag atoms. Temperature-accelerated retention time measurements were carried out to study the data retention performance of solvent engineering-based devices, as shown in Fig. 5E. The inset image shows that the linear fitting and the estimated retention time at 85°C can be extrapolated. Furthermore, from the linear fitting, the retention time at room temperature was obtained to be ~7 × 10⁹ s. The activation energy can be calculated as 1.15 eV. The retention time measured at 105°C of polycrystalline and monocryalline NW-based devices is compared in Fig. 5F. Polycrystalline MAPbCl₃ NW-based devices

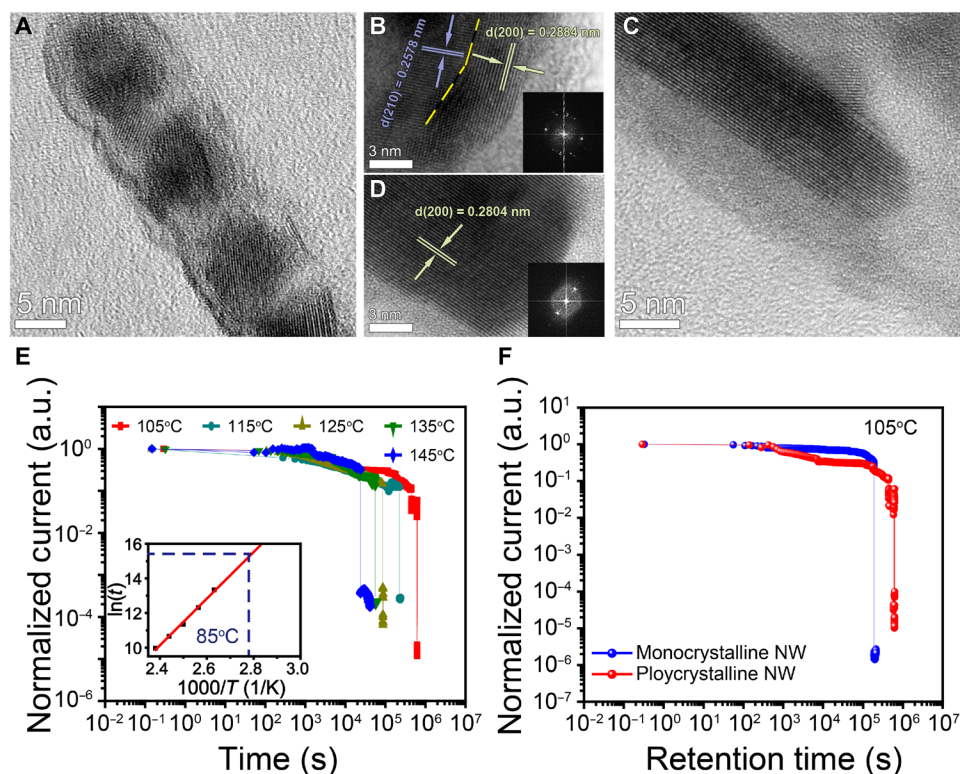


Fig. 5. TEM characterization and retention time comparison of polycrystalline NW-based devices and monocrystalline NW-based devices. (A) HRTEM of a single polycrystalline MAPbCl₃ NW. (B) Magnified HRTEM view of polycrystalline MAPbCl₃ NW showing varying lattice orientations, and inset shows corresponding fast Fourier transform (FFT) analysis. (C) HRTEM of a single monocrystalline MAPbCl₃ NW. (D) Magnified HRTEM view of monocrystalline MAPbCl₃ NW showing single lattice orientation, and inset shows corresponding FFT analysis. (E) Retention time of polycrystalline MAPbCl₃ NW-based devices. (F) Retention time comparison of MAPbCl₃ polycrystalline NWs and monocrystalline NW-based devices.

show the highest reported data retention time for organic-inorganic hybrid perovskite memories to the best of our knowledge. Table 1 gives a summary of data retention performance of the state-of-the-art organic-inorganic hybrid perovskite-based Re-RAM devices. Even when compared to all conventional types of Re-RAMs reported so far, the retention time performance of our device is among the ones in the premier shelf while having one of the fastest switching speed (see fig. S16) (24, 37–44, 51–57). The comparison of retention time performance for different kinds of previously reported Re-RAMs is shown in fig. S16A; all used the Arrhenius extrapolation method for estimating the retention time. Results show that polycrystalline MAPbCl₃ NW-based devices show much longer retention time than monocrystalline devices, which provide a practicable way to acquire a tunable data retention ability.

DISCUSSION

In summary, here, we report Re-RAM devices based on three-dimensional perovskite NW array. The unique NW array structure with laterally passivated PAM improved the material and electrical stability of the devices, also paving the way for future high-density storage. The devices exhibited ultralong retention time, bringing perovskite-based Re-RAMs at par with conventional NVMs in terms of temporal storage of data. We have also provided in-depth simulations and mechanistic study explaining the reason for ultra-high data retention and ultrafast switching speed and a subsequent

existing possible trade-off between the two. Meanwhile, the devices exhibited multilevel data retention ability, high ON/OFF ratio, and high endurance compared with state-of-the-art NVMs. All in all, the discoveries here herald the possibility of an ultralong temporal data retention-enabled and ultrafast operational speed-based Re-RAM system. Together with the proven down-scalability and ease of fabrication of perovskite NWs in the past, the new Re-RAM system may find important applications in future intelligent electronic systems.

MATERIALS AND METHODS

Device fabrication

PAM template fabrication

Aluminum chips with a dimension of 15 mm by 25 mm by 0.25 mm were used to fabricate the PAM template through the anodic anodization method reported previously (58). For a typical PAM template with a 1- μ m channel length and a 250-nm pore diameter fabrication process, the Al chips were first polished in an acidic solution (25% HClO₄ and 75 volume % absolute CH₃CH₂OH) for 3 min to clean the surface. Second, the Al sheets were anodized in a solution (deionized water: ethyleneglycol:H₃PO₄ = 200:100:1, by volume) under the voltage of 200 V for two times. Before the second anodization, the first time anodized layer was etched away by using a mixture of phosphoric acid [6 weight % (wt %) H₃PO₄ and 1.8 wt % CrO₃] for 20 min at 98°C to produce natural hexagonal ordering. For the 15-nm NW samples, 5 volume % H₂SO₄ at a voltage of 15 V was used for

Table 1. Data retention performance comparison of the state-of-the-art organic-inorganic hybrid perovskite-based devices. RT, room temperature.

Device structure	ON/OFF ratio	Retention time (s)	Reading voltage (V)	Report time (year)	Reference
ITO/MAPbI _{3-x} Cl _x /2D perovskite/Al	>10 ³	10 ⁴ /RT	0.25	2020	(19)
Al/RbPbBr ₃ /ITO/polyethylene	~10 ⁶	10 ⁴ /RT	0.4	2020	(20)
Au/PMMA/CsSnI ₃ /Pt	>10 ³	3 × 10 ³ /RT	0.02	2019	(21)
Au/CH ₃ NH ₃ PbI ₃ /Au	~10 ⁸	10 ⁴ /RT	0.05	2019	(22)
ITO/Cs ₂ AgBiBr ₆ /Au	~10 ⁴	10 ⁵ /RT	-1	2019	(23)
Au/(CH ₃ NH ₃) ₃ Bi ₂ I ₉ /ITO	>10 ⁴	10 ³ /RT	0.20	2018	(24)
Ag/PMMA/CsPBr ₃ QDs/PMMA/ITO/PET	~10 ⁵	4 × 10 ⁵ /RT	0.50	2018	(25)
Ag/CH ₃ NH ₃ PbI ₃ /Pt	>10 ⁶	1.1 × 10 ⁴ /RT	-	2016	(26)
Au/CH ₃ NH ₃ PbI _{3-x} Cl _x /FTO	>10 ²	10 ⁴ /RT	0.25	2015	(27)
Ag/MAPbCl ₃ monocrystalline NWs/Al	~10 ⁷	>10 ⁷ /RT	0.01		This work
Ag/MAPbCl ₃ monocrystalline NWs/Al	~10 ⁷	~9 × 10 ⁸ /RT *	0.01		This work
Ag/MAPbCl ₃ monocrystalline NWs/Al	~10 ⁷	>7 × 10 ⁵ /85 °C	0.01		This work
Ag/MAPbCl ₃ polycrystalline NWs/Al	~10 ⁷	~7 × 10 ⁹ /RT *	0.01		This work
Ag/MAPbCl ₃ polycrystalline NWs/Al	~10 ⁷	>6 × 10 ⁵ /105°C	0.01		This work

Retention time value is extrapolated from Arrhenius relation [$\ln(t) \propto E_a/kT$]. Value without "" is measured from real-time measurement.

the fabrication process. The length of the PAM channel was controlled by the second anodization time. In addition, the diameter of each channel was controlled by the anodization voltage. For ordered NW growth, Si molds were used to transfer the regular pattern on the polished Al chips and the succeeding PAM fabrication yielded ordered nanopore array.

NW-based devices fabricated by VSSR process

A voltage ramping-down process was used to thin the Al₂O₃ barrier layer of PAM down to ~4 nm carrying out in 0.2 M H₃PO₄ solution for the 250-nm-diameter devices. The Pb precursor was then deposited on the barrier thinned chips at the bottom of PAM channels. Perovskite NWs were successfully grown by a bottom-up VSSR process at 180°C when the Pb-electrodeposited PAM reacted with CH₃NH₃X (X = I, Br, and Cl) powders under the Ar carrier gas. The similar NW fabrication has been reported previously (13, 58). The NW-filled PAM surface was cleaned by ion milling under the condition of 100-V accelerating voltage for 1 hour. Four minutes of the VSSR regrowth process was carried out for interfacial repairing.

NW-based devices fabricated by solvent engineering

Precursor solution consisting of CH₃NH₃Cl and PbCl₂ dissolving in dimethyl sulfoxide (DMSO) (1.1 g/ml) with a 1:1 molar ratio was spin-coated on PAM, which was fabricated by 15-V anodization voltage. Ten minutes of annealing at 110°C was followed to support the MAPbCl₃ crystallization process.

Thin film-based devices fabricated by solvent engineering

Precursor solution consisting of CH₃NH₃Cl and PbCl₂ dissolved in DMSO (1.1 g/ml) with a 1:1 molar ratio was spin-coated on electropolished planar aluminum chips without any PAM layer. Twenty minutes of annealing at 100°C was followed to support the MAPbCl₃ crystallization process. For SEM morphology of MAPbI₃ and MAPbBr₃ shown in fig. S10, the precursor solution comprised CH₃NH₃X and PbX₂ with a molar ratio of 1:1 dissolved in *N,N'*-dimethylformamide (0.5 g/ml) and DMSO (1.1 g/ml), with other conditions remaining intact.

Electrode evaporation and device packaging

To fabricate Re-RAM devices, 100-nm layer of Ag was evaporated as the top electrode with an electrode area of 0.0314 cm² under the pressure of 5 × 10⁻⁴ Pa. For switching speed test device fabrication, 270-μm-wide rectangular strips of 50-nm-thick Ag were used as the top electrode. Al substrate was used as the bottom electrode. After the evaporation of the top contacts, wire bonding and NOA81 epoxy packaging were carried out.

MAPbCl₃ NW extraction

Single NWs for TEM characterization were produced by a mechanical grinding and sonication process. To get NWs formed by the VSSR process, HgCl₂ etching was used to obtain a free-standing Pb-deposited PAM membrane first. Then, the VSSR process and electrode evaporation were followed to finish the device fabrication.

Afterward, the samples were mechanically pulverized and dissolved in toluene and further sonicated for 20 min. The single NW would finally be stripped from PAM and dispersed uniformly into solvent.

Reliability test

Eighty percent RH was maintained by KCl saturated salt solution at 85°C in a closed oven.

Material characterization

SEM and EDS images were obtained from SEM JEOL JSM-7100F. High-resolution TEM and EDS studies were carried out by TEM JEOL (2010). XRD measurement for deciphering the crystal structure was performed with a Bruker D8 X-ray 22 diffractometer.

Electrical measurements

The cyclic *I-V* characteristics and endurance of the memory devices were measured by Keithley 4200-SCS and 4225 PMU, and Gamry Potentiostat SG 300, respectively. The retention time was measured by Keithley 2450 with homebuilt LABVIEW programs, while the device was mounted on a Lakeshore probe station equipped with a 336 temperature controller. The single pulse generated for switching speed measurement was produced with a Picosecond Pulse Labs Model 10070A pulse generator, and the resistance of the device was monitored with a Keithley 2600 source meter assisted by homebuilt LABVIEW programs. A DPO 70804C oscilloscope was used to observe the input pulses.

Ag activation energy simulations

All first-principles calculations in this work were performed using VASP (59) with the projected augmented wave approach (60). The generalized gradient approximation Perdew-Berke-Ernzerhof was adopted for the exchange-correlation functional. The Brillouin zone was sampled by a $3 \times 3 \times 3$ Monkhorst-Pack grid, and the energy cutoff was set to 520 eV. All geometry structures were fully relaxed until the convergence criteria of energy and forces of 10^{-5} and 0.02 eV/Å were reached, respectively. All energy cutoff and *k*-points have been tested until the energy reaches its convergence. The fully optimized structures were used as the initial configurations for the subsequent calculations. The migration barriers for the Ag atom diffusion in $\text{Ag}_{0.5}\text{MAPbX}_3$ and AgMAPbX_3 perovskites were calculated using the climbing nudged band method (CI-NEB) (61) through the codes of transition state tools for VASP (VTST) codes (62), in compliance with VASP. All the transitional points were propagated along the migration direction in a series of traced diffusion ribbon, with all unconstrained degrees of freedom relaxed at each step. During the NEB calculations, the Pb cations and the halide anions were fixed. MA was relaxed because of the wire-like alignment and light weight. The same method has been used before in previous reports (63, 64).

SUPPLEMENTARY MATERIALS

Supplementary material for this article is available at <https://science.org/doi/10.1126/sciadv.abg3788>

REFERENCES AND NOTES

- D. Ielmini, R. Waser, *Resistive Switching: From Fundamentals of Nanoionic Redox Processes to Memristive Device Applications* (John Wiley & Sons, 2015).
- Y. Chen, ReRAM: History, status, and future. *IEEE Trans. Electron Devices* **67**, 1420–1433 (2020).
- B. Govoreanu, G. Kar, Y. Y. Chen, V. Paraschiv, S. Kubicek, A. Fantini, I. Radu, L. Goux, S. Clima, R. Degraeve, N. Jossart, O. Richard, T. Vandeweyer, K. Seo, P. Hendrickx, G. Pourtois, H. Bender, L. Altimime, D. Wouters, J. A. Kittl, M. Jurczak, $10 \times 10 \text{ nm}^2$ Hf/HfO₂ crossbar resistive RAM with excellent performance, reliability and low-energy operation, in *2011 International Electron Devices Meeting (IEEE, 2011)*, pp. 31.36.31–31.36.34.
- Y.-B. Kim, S. R. Lee, D. Lee, C. B. Lee, M. Chang, J. H. Hur, M. J. Lee, G. S. Park, C. J. Kim, U. I. Chung, Bi-layered RRAM with unlimited endurance and extremely uniform switching, in *2011 Symposium on VLSI Technology—Digest of Technical Papers (IEEE, 2011)*, pp. 52–53.
- Z. Wei, T. Takagi, Y. Kanzawa, Y. Katoh, T. Ninomiya, K. Kawai, S. Muraoka, S. Mitani, K. Katayama, S. Fujii, R. Miyanaga, Y. Kawashima, T. Mikawa, K. Shimakawa, K. Aono, Demonstration of high-density ReRAM ensuring 10-year retention at 85°C based on a newly developed reliability model, in *2011 International Electron Devices Meeting (IEEE, 2011)*, pp. 31.34.31–31.34.34.
- F. Zhang, H. Zhang, S. Krylyuk, C. A. Milligan, Y. Zhu, D. Y. Zemlyanov, L. A. Bendersky, B. P. Burton, A. V. Davydov, J. Appenzeller, Electric-field induced structural transition in vertical MoTe₂- and Mo_{1-x}W_xTe₂-based resistive memories. *Nat. Mater.* **18**, 55–61 (2019).
- M. Wang, S. Cai, C. Pan, C. Wang, X. Lian, Y. Zhuo, K. Xu, T. Cao, X. Pan, B. Wang, S. J. Liang, J. J. Yang, P. Wang, F. Miao, Robust memristors based on layered two-dimensional materials. *Nat. Electron.* **1**, 130–136 (2018).
- C. Gu, J.-S. Lee, Flexible hybrid organic-inorganic perovskite memory. *ACS Nano* **10**, 5413–5418 (2016).
- N. J. Jeon, J. H. Noh, W. S. Yang, Y. C. Kim, S. Ryu, J. Seo, S. I. Seok, Compositional engineering of perovskite materials for high-performance solar cells. *Nature* **517**, 476–480 (2015).
- K.-G. Lim, S. Ahn, Y.-H. Kim, Y. Qi, T.-W. Lee, Universal energy level tailoring of self-organized hole extraction layers in organic solar cells and organic-inorganic hybrid perovskite solar cells. *Energ. Environ. Sci.* **9**, 932–939 (2016).
- Q. Zhang, M. M. Tavakoli, L. Gu, D. Zhang, L. Tang, Y. Gao, Y. Lin, S. F. Leung, S. Poddar, Y. Fu, Z. Fan, Efficient metal halide perovskite light-emitting diodes with significantly improved light extraction on nanophotonic substrates. *Nat. Commun.* **10**, 727 (2019).
- Y. Wang, Z. Lv, L. Zhou, X. Chen, J. Chen, Y. Zhou, V. A. L. Roy, S.-T. Han, Emerging perovskite materials for high density data storage and artificial synapses. *J. Mater. Chem. C* **6**, 1600–1617 (2018).
- A. Waleed, M. M. Tavakoli, L. Gu, Z. Wang, D. Zhang, A. Manikandan, Q. Zhang, R. Zhang, Y.-L. Chueh, Z. Fan, Lead-free perovskite nanowire array photodetectors with drastically improved stability in nanoengineering templates. *Nano Lett.* **17**, 523–530 (2017).
- H. Wang, X. B. Yan, Overview of resistive random access memory (RRAM): Materials, filament mechanisms, performance optimization, and prospects. *Phys. Status Solidi Rapid Res. Lett.* **13**, 1900073 (2019).
- D. Lim, M. Kim, Y. Kim, S. Kim, Memory characteristics of silicon nanowire transistors generated by weak impact ionization. *Sci. Rep.* **7**, 12436 (2017).
- C. Cagli, F. Nardi, B. Harteneck, Z. Tan, Y. Zhang, Resistive-switching crossbar memory based on Ni-NiO core-shell nanowires. *Small* **7**, 2899–2905 (2011).
- K.-M. Persson, M. S. Ram, O.-P. Kilpi, M. Borg, L.-E. Wernersson, Cross-point arrays with low-power ITO-HfO₂ resistive memory cells integrated on vertical III-V nanowires. *Adv. Electron. Mater.* **6**, 2000154 (2020).
- Q. Zhang, D. Zhang, L. Gu, K. Tsui, S. Poddar, Y. Fu, L. Shu, Z. Fan, Three-dimensional perovskite nanophotonic wire array-based light-emitting diodes with significantly improved efficiency and stability. *ACS Nano* **14**, 1577–1585 (2020).
- F. Xia, Y. Xu, B. Li, W. Hui, S. Zhang, L. Zhu, Y. Xia, Y. Chen, W. Huang, Improved performance of CH₃NH₃PbI_{3-x}Cl_x resistive switching memory by assembling 2D/3D perovskite heterostructures. *ACS Appl. Mater. Interfaces* **12**, 15439–15445 (2020).
- U. Das, A. Nyayban, B. Paul, A. Barman, P. Sarkar, A. Roy, Compliance current-dependent dual-functional bipolar and threshold resistive switching in all-inorganic rubidium lead-bromide perovskite-based flexible device. *ACS Appl. Electron. Mater.* **2**, 1343–1351 (2020).
- J. S. Han, Q. V. Le, J. Choi, H. Kim, S. G. Kim, K. Hong, C. W. Moon, T. L. Kim, S. Y. Kim, H. W. Jang, Lead-free all-inorganic cesium tin iodide perovskite for filamentary and interface-type resistive switching toward environment-friendly and temperature-tolerant nonvolatile memories. *ACS Appl. Mater. Interfaces* **11**, 8155–8163 (2019).
- K. Kang, H. Ahn, Y. Song, W. Lee, J. Kim, Y. Kim, D. Yoo, T. Lee, High-performance solution-processed organo-metal halide perovskite unipolar resistive memory devices in a cross-bar array structure. *Adv. Mater.* **31**, e180484 (2019).
- X. F. Cheng, W. H. Qian, J. Wang, C. Yu, J. H. He, H. Li, Q. F. Xu, D. Y. Chen, N. J. Li, J. M. Lu, Environmentally robust memristor enabled by lead-free double perovskite for high-performance information storage. *Small* **15**, e1905731 (2019).
- B. Hwang, J. S. Lee, Lead-free, air-stable hybrid organic-inorganic perovskite resistive switching memory with ultrafast switching and multilevel data storage. *Nanoscale* **10**, 8578–8584 (2018).
- Y. Wang, Z. Lv, Q. Liao, H. Shan, J. Chen, Y. Zhou, L. Zhou, X. Chen, V. A. L. Roy, Z. Wang, Z. Xu, Y. J. Zeng, S. T. Han, Synergies of electrochemical metallization and valance change in all-inorganic perovskite quantum dots for resistive switching. *Adv. Mater.* **30**, e1800327 (2018).
- J. Choi, S. Park, J. Lee, K. Hong, D. Kim, C. Moon, G. Park, J. Suh, J. Hwang, S. Kim, H. Jung, N. Park, S. Han, K. Nam, H. Jang, Organolead halide perovskites for low operating voltage multilevel resistive switching. *Adv. Mater.* **28**, 6562–6567 (2016).

27. E. J. Yoo, M. Lyu, J. H. Yun, C. J. Kang, Y. J. Choi, L. Wang, Resistive switching behavior in organic-inorganic hybrid $\text{CH}_3\text{NH}_3\text{Pb}_{1-x}\text{Cl}_x$ perovskite for resistive random access memory devices. *Adv. Mater.* **27**, 6170–6175 (2015).
28. A. Waleed, M. M. Tavakoli, L. Gu, S. Hussain, D. Zhang, S. Poddar, Z. Wang, R. Zhang, Z. Fan, All inorganic cesium lead iodide perovskite nanowires with stabilized cubic phase at room temperature and nanowire array-based photodetectors. *Nano Lett.* **17**, 4951–4957 (2017).
29. L. Gu, D. Zhang, M. Kam, Q. Zhang, S. Poddar, Y. Fu, X. Mo, Z. Fan, Significantly improved black phase stability of FAPbI_3 nanowires via spatially confined vapor phase growth in nanoporous templates. *Nanoscale* **10**, 15164–15172 (2018).
30. D. Zhang, L. Gu, Q. Zhang, Y. Lin, D. H. Lien, M. Kam, S. Poddar, E. C. Garnett, A. Javey, Z. Fan, Increasing photoluminescence quantum yield by nanophotonic design of quantum-confined halide perovskite nanowire arrays. *Nano Lett.* **19**, 2850–2857 (2019).
31. G. Maculan, A. D. Sheikh, A. L. Abdelhady, M. I. Saidaminov, M. A. Haque, B. Murali, E. Alarousu, O. F. Mohammed, T. Wu, O. M. Bakr, $\text{CH}_3\text{NH}_3\text{PbCl}_3$ single crystals: Inverse temperature crystallization and visible-blind UV-photodetector. *J. Phys. Chem. Lett.* **6**, 3781–3786 (2015).
32. S. G. Kim, Q. Van Le, J. S. Han, H. Kim, M. J. Choi, S. A. Lee, T. L. Kim, S. B. Kim, S. Y. Kim, H. W. Jang, Dual-phase all-inorganic cesium halide perovskites for conducting-bridge memory-based artificial synapses. *Adv. Funct. Mater.* **29**, 1906686 (2019).
33. J. S. Han, Q. V. Le, J. Choi, K. Hong, C. W. Moon, T. L. Kim, H. Kim, S. Y. Kim, H. W. Jang, Air-stable cesium lead iodide perovskite for ultra-low operating voltage resistive switching. *Adv. Funct. Mater.* **28**, 1705783 (2018).
34. F. Zeng, Y. Guo, W. Hu, Y. Tan, X. Zhang, J. Feng, X. Tang, Opportunity of the lead-free all-inorganic $\text{Cs}_2\text{Cu}_2\text{I}_2$ perovskite film for memristor and neuromorphic computing applications. *ACS Appl. Mater. Interfaces* **12**, 23094–23101 (2020).
35. R. Waser, R. Dittmann, G. Staikov, K. Szot, Redox-based resistive switching memories—nanoionic mechanisms, prospects, and challenges. *Adv. Mater.* **21**, 2632–2663 (2009).
36. Y. Yang, P. Gao, S. Gaba, T. Chang, X. Pan, W. Lu, Observation of conducting filament growth in nanoscale resistive memories. *Nat. Commun.* **3**, 732 (2012).
37. S. Pi, M. Ghadiri-Sadrabadi, J. C. Bardin, Q. Xia, Nanoscale memristive radiofrequency switches. *Nat. Commun.* **6**, 7519 (2015).
38. C. Cagli, D. Ielmini, F. Nardi, A. L. Lacaita, Evidence for threshold switching in the set process of NiO-based RRAM and physical modeling for set, reset, retention and disturb prediction, in *2008 IEEE International Electron Devices Meeting (IEEE, 2008)*, pp. 1–4.
39. Z. Wang, Z. Jiang, X. Zheng, S. Fong, H.-Y. Chen, H.-S. P. Wong, Y. Nishi, Ultrafast accelerated retention test methodology for RRAM using micro thermal stage. *IEEE Electron Device Lett.* **38**, 863–866 (2017).
40. S. Choi, J. Lee, S. Kim, W. D. Lu, Retention failure analysis of metal-oxide based resistive memory. *Appl. Phys. Lett.* **105**, 113510 (2014).
41. P. Zhou, H. J. Wan, Y. L. Song, M. Yin, H. B. Lv, Y. Y. Lin, S. Song, R. Huang, J. G. Wu, M. H. Chi, A systematic investigation of $\text{TiN}/\text{Cu}_x\text{O}/\text{Cu}$ RRAM with long retention and excellent thermal stability, in *2009 IEEE International Memory Workshop (IEEE, 2009)*, pp. 1–2.
42. Y. Pang, H. Wu, B. Gao, N. Deng, D. Wu, R. Liu, S. Yu, A. Chen, H. Qian, Optimization of RRAM-based physical unclonable function with a novel differential read-out method. *IEEE Electron Device Lett.* **38**, 168–171 (2017).
43. M. C. Wu, Y. W. Lin, W. Y. Jang, C. H. Lin, T. Y. Tseng, Low-power and highly reliable multilevel operation in ZrO_2 1T1R RRAM. *IEEE Electron Device Lett.* **32**, 1026–1028 (2011).
44. B. Govoreanu, A. Redolfi, L. Zhang, C. Adelmann, M. Popovici, S. Clima, H. Hody, V. Parasciv, I. P. Radu, A. Franquet, J. C. Liu, J. Swerts, O. Richard, H. Bender, L. Altimime, M. Jurczak, Vacancy-modulated conductive oxide resistive RAM (VMCO-RRAM): An area-scalable switching current, self-compliant, highly nonlinear and wide on/off-window resistive switching cell, in *2013 IEEE International Electron Devices Meeting (IEEE, 2013)*, pp. 10.12.11–10.12.14.
45. S. Choi, S. H. Tan, Z. Li, Y. Kim, C. Choi, P. Y. Chen, H. Yeon, S. Yu, J. Kim, SiGe epitaxial memory for neuromorphic computing with reproducible high performance based on engineered dislocations. *Nat. Mater.* **17**, 335–340 (2018).
46. J. C. Bachman, S. Mui, A. Grimaud, H. H. Chang, N. Pour, S. F. Lux, O. Paschos, F. Maglia, S. Lupart, P. Lamp, L. Giordano, Y. Shao-Horn, Inorganic solid-state electrolytes for lithium batteries: Mechanisms and properties governing ion conduction. *Chem. Rev.* **116**, 140–162 (2016).
47. Z. Xu, X. Chen, R. Chen, X. Li, H. Zhu, Anion charge and lattice volume dependent lithium ion migration in compounds with fcc anion sublattices. *NPJ Comput. Mater.* **6**, 47 (2020).
48. D. A. Egger, L. Kronik, Role of dispersive interactions in determining structural properties of organic-inorganic halide perovskites: Insights from first-principles calculations. *J. Phys. Chem. Lett.* **5**, 2728–2733 (2014).
49. Y. R. Luo, J. A. Kerr, Bond dissociation energies. *CRC Handb. Chem. Phys.* **89**, 89 (2012).
50. G. P. Nagabhushana, R. Shivaramaiah, A. Navrotsky, Direct calorimetric verification of thermodynamic instability of lead halide hybrid perovskites. *Proc. Natl. Acad. Sci. U.S.A.* **113**, 7717–7721 (2016).
51. B. J. Choi, A. C. Torrezan, J. P. Strachan, P. G. Kotula, A. J. Lohn, M. J. Marinella, Z. Y. Li, R. S. Williams, J. J. Yang, High-speed and low-energy nitride memristors. *Adv. Funct. Mater.* **26**, 5290–5296 (2016).
52. A. C. Torrezan, J. P. Strachan, G. Medeiros-Ribeiro, R. S. Williams, Sub-nanosecond switching of a tantalum oxide memristor. *Nanotechnology* **22**, 485203 (2011).
53. U. Böttger, M. von Witzleben, V. Havel, K. Fleck, V. Rana, R. Waser, S. Menzel, Picosecond multilevel resistive switching in tantalum oxide thin films. *Sci. Rep.* **10**, 16391 (2020).
54. B. J. Choi, A. C. Torrezan, K. J. Norris, F. Miao, J. P. Strachan, M. X. Zhang, D. A. Ohlberg, N. P. Kobayashi, J. J. Yang, R. S. Williams, Electrical performance and scalability of Pt dispersed SiO_2 nanometallic resistance switch. *Nano Lett.* **13**, 3213–3217 (2013).
55. H. Y. Lee, Y. S. Chen, P. S. Chen, P. Y. Gu, Y. Y. Hsu, S. M. Wang, W. H. Liu, C. H. Tsai, S. S. Sheu, P. C. Chiang, W. P. Lin, C. H. Lin, W. S. Chen, F. T. Chen, C. H. Lien, M. J. Tsai, Evidence and solution of over-RESET problem for HfO_2 based resistive memory with sub-ns switching speed and high endurance, in *2010 International Electron Devices Meeting (IEEE, 2010)*, pp. 19.17.11–19.17.14.
56. H.-S. P. Wong, H.-Y. Lee, S. Yu, Y.-S. Chen, Y. Wu, P.-S. Chen, B. Lee, F. T. Chen, M.-J. Tsai, Metal-oxide RRAM. *Proc. IEEE* **100**, 1951–1970 (2012).
57. S. Y. Wang, D. Y. Lee, T. Y. Huang, J. W. Wu, T. Y. Tseng, Controllable oxygen vacancies to enhance resistive switching performance in a ZrO_2 -based RRAM with embedded Mo layer. *Nanotechnology* **21**, 495201 (2010).
58. L. Gu, M. M. Tavakoli, D. Zhang, Q. Zhang, A. Waleed, Y. Xiao, K. H. Tsui, Y. Lin, L. Liao, J. Wang, Z. Fan, 3D arrays of 1024-pixel image sensors based on lead halide perovskite nanowires. *Adv. Mater.* **28**, 9713–9721 (2016).
59. G. Kresse, J. Furthmüller, Efficient iterative schemes for *ab initio* total-energy calculations using a plane-wave basis set. *Phys. Rev. B* **54**, 11169–11186 (1996).
60. P. E. Blöchl, Projector augmented-wave method. *Phys. Rev. B* **50**, 17953–17979 (1994).
61. G. Henkelman, B. P. Uberuaga, H. Jónsson, A climbing image nudged elastic band method for finding saddle points and minimum energy paths. *J. Phys. Chem. B* **113**, 9901–9904 (2000).
62. G. Henkelman, H. Jónsson, Improved tangent estimate in the nudged elastic band method for finding minimum energy paths and saddle points. *J. Chem. Phys.* **113**, 9978–9985 (2000).
63. Z. Xu, H. Zhu, Anion charge and lattice volume maps for searching lithium superionic conductors. *Chem. Mater.* **32**, 4618–4626 (2020).
64. G. Sahu, Z. Lin, J. Li, Z. Liu, N. Dudney, C. Liang, Air-stable, high-conduction solid electrolytes of arsenic-substituted Li_4SnS_4 . *Energ. Environ. Sci.* **7**, 1053–1058 (2014).

Acknowledgments: We thank R. Ho, Y. Zhang, and A. H. K. Wong from Material and Characterization Preparation Facility (MCPF) at HKUST for technically assisting in acquiring TEM images and SEM images. **Funding:** This work was supported by Science and Technology Plan of Shenzhen (JCYJ20170818114107730 and JCYJ20180306174923335), the General Research Fund (project nos. 16309018 and 16214619) from the Hong Kong Research Grant Council, Innovation Technology Fund (GHP/014/19S2), Guangdong-Hong Kong-Macao Intelligent Micro-Nano Optoelectronic Technology Joint Laboratory (project no. 2020B1212030010), HKUST Fund of Nanhai (grant no. FSNH-18FYTR101), and Foshan Innovative and Entrepreneurial Research Team Program (2018IT100031). We also acknowledge the support from the Center for 1D/2D Quantum Materials and the State Key Laboratory of Advanced Displays and Optoelectronics Technologies at HKUST. **Author contributions:** Z.F., Y.Zha., and S.P. conceptualized the experiments and analyzed the results. Y.Zha. systematically studied the retention time and switching speed characteristics in different Re-RAM systems. S.P. pioneered the beginning work based on MAPbI_3 NW Re-RAM devices, performed the TEM sample preparations and imaging, and helped with the electrical characterizations. B.H. and H.H. did in-depth simulation studies based on density functional theory (DFT) method. L.G. carried the characterization of SEM images. Z.S., S.Y., and S.Z. helped with the speed test for the memory device. Q.Z. and Y.Zho. helped with device fabrication. G.S. helped with device electrical characterization. All authors participated in manuscript writing and articulation. **Competing interests:** Z.F. is an inventor on a patent application related to this work (no. 63221017, filed on 13 July 2021). The authors declare no other competing interests. **Data and materials availability:** All data needed to evaluate the conclusions in the paper are present in the paper and/or the Supplementary Materials.

Submitted 1 January 2021
Accepted 14 July 2021
Published 3 September 2021
10.1126/sciadv.abg3788

Citation: Y. Zhang, S. Poddar, H. Huang, L. Gu, Q. Zhang, Y. Zhou, S. Yan, S. Zhang, Z. Song, B. Huang, G. Shen, Z. Fan, Three-dimensional perovskite nanowire array-based ultrafast resistive RAM with ultralong data retention. *Sci. Adv.* **7**, eabg3788 (2021).

Three-dimensional perovskite nanowire array–based ultrafast resistive RAM with ultralong data retention

Yuting Zhang Swapnadeep Poddar He Huang Leilei Gu Qianpeng Zhang Yu Zhou Shuai Yan Sifan Zhang Zhitang Song Baoling Huang Guozhen Shen Zhiyong Fan

Sci. Adv., 7 (36), eabg3788. • DOI: 10.1126/sciadv.abg3788

View the article online

<https://www.science.org/doi/10.1126/sciadv.abg3788>

Permissions

<https://www.science.org/help/reprints-and-permissions>

Use of this article is subject to the [Terms of service](#)